RESEARCH ARTICLE
SPACE PHYSICS: MAGNETOSPHERIC PHYSICS

Earth and Planetary Physics
9: 946–954, 2025
doi: 10.26464/epp2025072

A semi-empirical approach to simulating the *Dst* index in global MHD models of Earth's magnetosphere

JiaWen Yue[1,2], XiaoCheng Guo[1,2*], YuXian Wang[1], and Chi Wang[1,2]

[1]Key Laboratory of Solar Activity and Space Weather, National Space Science Center, Chinese Academy of Sciences, Beijing 100190, China;

[2]College of Earth and Planetary Sciences, University of Chinese Academy of Sciences, Chinese Academy of Sciences, Beijing 100049, China

Key Points:

- A semi-empirical *Dst* model has been developed for the calculation of *Dst* index in a global MHD simulation of Earth's magnetosphere.
- This model employs an empirical formula to evaluate the contribution from the ring current system.
- The numerical results indicate the successful application of the *Dst* model during the magnetic storm events.

Citation: Yue, J. W., Guo, X. C., Wang, Y. X., and Wang, C. (2025). A semi-empirical approach to simulating the *Dst* index in global MHD models of Earth's magnetosphere. *Earth Planet. Phys.*, *9*(4), 946–954. http://doi.org/10.26464/epp2025072

Abstract: The *Dst* index has been commonly used to measure the geomagnetic effectiveness of magnetic storm events for several decades. Based on Burton's empirical *Dst* model and the global magneto-hydrodynamic (MHD) simulation of Earth's magnetosphere, here we proposed a semi-empirical model to forecast the *Dst* index during geomagnetic storms. In this model, the ring current contribution to the *Dst* index is derived from Burton's model, while the contributions from other current systems are obtained from the global MHD simulation. In order to verify the model accuracy, a number of recent magnetic storm events are tested and the simulated *Dst* index is compared with the observation through the correlation coefficient (CC), prediction efficiency (PE), root mean square error (RMSE) and central root mean square error (CRMSE). The results indicate that, in the context of moderate and intense geomagnetic storm events, the semi-empirical model performs well in global MHD simulations, showing relatively higher CC and PE, and lower RMSE and CRMSE compared to those from the empirical model. Compared with the physics-based ring current models, this model inherits the advantage of fast processing from the empirical model, and easy implementation in a global MHD model of Earth's magnetosphere. Therefore, it is suitable for the *Dst* estimation under a context of a global MHD simulation.

Keywords: global MHD; *Dst* index; SYM-*H* index; semi-empirical model; Earth's magnetosphere

1. Introduction

The *Dst* index is the most widely used index to describe the intensity of magnetic storm activity and is of great significance in the study of geomagnetic disturbances and storms. The basic concept of the *Dst* index was first proposed by Sugiura (1960). It is obtained by subtracting the average variation during the calm period from the horizontal components of the geomagnetic field measured by the four low latitude observatories (Sugiura et al., 1964). These observatories are chosen to minimize effects from auroral and equatorial electric currents, and their longitudes are roughly evenly distributed around the globe. However, the time resolution of the *Dst* index is only one hour, which appears relatively large to describe some geomagnetic events. As an alternative, the SYM-*H* index can be viewed as an upgraded *Dst* index with one minute resolution and deviations typically less than 20 nT for moderate and intense storms (Wanliss and Showalter, 2006). Different from the *Dst* index, the SYM-*H* index is calculated using data from six ground magnetometer stations in low and mid latitudes with uniformly distributed longitudes from the global equatorial region (Iyemori, 1990).

Physically, the magnitude of the *Dst* index is a measure of the intensity of the equatorial ring current and can usually reflect the intensity of a magnetic storm. Burton et al. (1975) classified magnetic storms into four levels based on the minimum value of the *Dst* index: minor storms with a minimum value of −30 to −50 nT, moderate storms with a minimum value of −50 to −100 nT, intense storms with a minimum value of −100 to −200 nT, and super storms with a minimum value exceeding −200 nT. Accurately predicting the *Dst* index is of great value for magnetic storm and the related space weather forecasting research.

Various methods have been developed for forecasting the *Dst* index, by using observed solar wind parameters as inputs. Typically, they can be classified as three types, including empirical formula, machine-learning methods, and physics-based models. Among them, empirical formula models are most popularly used for its relative simplicity for the numerical implementation. In

First author: J. W. Yue, jwyue@swl.ac.cn
Correspondence to: X. C. Guo, xcguo@swl.ac.cn
Received 14 JAN 2025; Accepted 18 MAR 2025.
First Published online 20 MAY 2025.

early research, Burton et al. (1975) proposed an empirical formula for calculating the *Dst* index, using the solar wind parameter related terms as the coefficients in the differential equation, factoring in particle injections from the plasma sheet into the inner magnetosphere, and highlighting the crucial role of the southward component of the interplanetary magnetic field (IMF) in the calculation. Later, several extended versions of the empirical model have been derived and applied in the relevant fields (Lundstedt et al., 2002; Park et al., 2021), and since Burton et al. (1975), there have been many studies based on this empirical formula (O'Brien and McPherron, 2000; Wang CB et al., 2003).

Machine learning and neural network techniques have been extensively applied to the modeling and prediction of the *Dst* index (Lu JY et al., 2016; Camporeale, 2019; Xu WW et al., 2023). As early as the 1990s, several attempts were made to utilize neural networks for *Dst* index prediction (Lundstedt and Wintoft, 1994; Gleisner et al., 1996; Wu JG and Lund-stedt, 1997; Kugblenu et al., 1999). Jankovičová et al. (2002) employed a fully connected neural network to forecast the *Dst* index, developing a model that could predict the index two hours ahead using ACE data. Lundstedt et al. (2002) studied the response characteristics and decay of solar wind dynamic pressure alterations and ring current injections, discovering that during reversals of the interplanetary magnetic field to a southward orientation, the rate of ring current injection is directly proportional to the solar wind dynamic pressure. They applied this finding to the prediction of the *Dst* index, enhancing the accuracy of forecasts. Caswell (2014) utilized components of the IMF, solar wind proton density, plasma velocity, and plasma flow pressure to predict the *Dst* index one hour in advance. Lazzús et al. (2017) introduced an Artificial Neural Network (ANN) model that achieved higher precision in *Dst* index predictions, with lead times ranging from 1 to 6 hours. Similar work based on ANN model has been carried out for a better prediction accuracy and stability (Lethy et al., 2018; Xu SB et al., 2020; Park et al., 2021).

The physics-based model typically solves the first-principle equations to describe dynamics of ring current and forecast the induced *Dst* index. Some models employ the Dessler–Parker–Scopke equation to transform the total energy within the simulated ring current into Dst^*, and then calculate the anticipated *Dst* index, incorporating corrections for magnetopause currents based on the dynamic pressure exerted by the solar wind (Dessler and Parker, 1959; Sckopke, 1966). The Rice Convection Model (RCM) describes the electrodynamics of inner magnetospheric plasma effectively (Wolf et al., 1991; Toffoletto et al., 2001). It employs Hilmer and Voigt's magnetic field descriptions (Hilmer and Voigt, 1995) in conjunction with either the Siscoe-Hill (Siscoe, 1982; Hill, 1984) or Weimer (Weimer, 2005) electric field models. The model calculates the field-aligned current using the Vasyliunas equation (Vasyliunas, 1970), based on the pressure gradient of the magnetospheric plasma. This current then determines the ionospheric potential and electric field, which are subsequently mapped back to the inner magnetosphere to complete the calculation loop. This process enables the calculation of the ring current's energy. Other inner magnetospheric models for simulating ring current dynamics include the RAM-SCB (Jordanova et al., 2010), CRCM (Buzulukova et al., 2010), and WINDMI models (Horton and Doxas, 1998). The RAM-SCB is an open-source simulation code that models the evolution of major ion species and electrons across various parameters such as azimuth, radial distance, energy, pitch angle, and the *Dst* index (Morley et al., 2023). On the other hand, the CRCM model provides accurate predictions of the *Dst* index for Coronal Mass Ejection (CME)-driven storms, yet it underestimates this index for Co-rotating Interaction Region (CIR)-driven storms, this discrepancy could result in a potential overestimation of up to half of the total ring current energy due to limitations in modeling the static magnetic field (Cramer et al., 2013). Lastly, WINDMI is a low-order, nonlinear ring current model capable of generating outputs for both the geomagnetic westward auroral electrojet (AL) index and the *Dst* index (Spencer et al., 2018).

Global magneto-hydrodynamic (MHD) models of Earth's magnetosphere can simulate the *Dst* index by combining current densities at various locations in the magnetosphere with the Biot–Savart formula to calculate the magnetic perturbation at Earth's center. However, these models can not simulate the ring current effectively, as they cannot capture the drift motion of charged particles in the inner magnetosphere. Therefore, an inner magnetosphere model must be integrated into global MHD models to more accurately simulate the *Dst* index. Examples of such global MHD models include BATSRUS (Tóth et al., 2005), OpenGGCM (Raeder et al., 2001), and LFM (Lyon et al., 2004). The BATSRUS model, for instance, is available in versions coupled with both the RCM (De Zeeuw et al., 2004) and the CRCM (Buzulukova et al., 2010). When integrated with an inner magnetosphere model, BATSRUS significantly improves its ability to replicate *Dst* values during magnetic storms, as it has been unable to reach a *Dst* value below −30 nT without this component (Liemohn et al., 2018). The European Heliospheric Forecasting Information Asset, when coupled with OpenGGCM, demonstrates effective predictions of geomagnetic disturbance indices, thereby enhancing space weather forecasting capabilities (Maharana et al., 2021). Rastätter et al. (2013) conducted a comprehensive review and analysis of the performance of these statistical and physics-based models in calculating the *Dst* index.

Instead of incorporating an inner magnetospheric model, here we attempt to integrate an empirical formula into a global MHD model of Earth's magnetosphere to simulate the *Dst* index. The structure of this paper is as follows: Section 2 introduces the methodology for calculating the *Dst* index, which includes both the global MHD model and the empirical formula. Section 3 outlines the specific events and datasets used in our analysis. Section 4 presents the simulation results, followed by a discussion of these events. Finally, Section 5 summarizes the conclusion.

2. Methodology

2.1 *Dst* Index in a Global MHD Model

The *Dst* index quantifies the intensity of general geomagnetic activity on low-latitude ground, and is used to estimate the energy density of the ring current near Earth. However, other magnetospheric current systems, such as dayside magnetopause currents and nightside tail currents can cause field perturbations on ground as well, may secondly contribute to the *Dst* index as the previous investigation reported (Turner et al., 2000). A revised version of the PPMLR-MHD model (Hu YQ et al., 2007) is applied in this work, in which an extension of HLL-type Riemann solver designed for the decomposition of intrinsic magnetic field is used to update the numerical flux at cell interfaces in a MUSCL numerical scheme (Guo XC, 2015; Guo XC et al., 2016). During the simulation, the magnetic field $\boldsymbol{B}$ at any given grid point is numerically updated at each time step through the time-dependent MHD equations, the magnetospheric current systems are directly calculated from the distortion of geomagnetic field caused by the continuous solar wind pressing from the upstream. The current density $\boldsymbol{j}$ is then obtained through the normalized relation $\boldsymbol{j} = \nabla \times \boldsymbol{B}$, containing the large-scale magnetopause, field-aligned, and tail currents. However, the ring currents are not generated because the gradient and curvature drift motions for charged particles can not be reproduced in a single-fluid MHD approximation.

For *Dst* index, here we do not consider the exact locations of the four major geomagnetic observatories; instead, the magnetic field perturbations at Earth's center are used to represent the averaged geomagnetic disturbances in the equatorial plane on ground, and the corresponding north–south axis component of the geomagnetic perturbation is defined as the *Dst* index, following the similar approach taken by the previous researchers in global MHD simulations (Rastätter et al., 2013; Liemohn et al., 2018). Using Biot-Savart's Law, the estimated *Dst* index Dst_{MHD} is expressed as the z component of the magnetic field perturbation in the center of GSM coordinate system,

$$Dst_{\text{MHD}} = \delta \boldsymbol{B}_z = \frac{1}{4\pi} \sum \frac{\boldsymbol{j} \times \boldsymbol{R}}{R^3} \Delta V, \tag{1}$$

where $\boldsymbol{R}$ is the spatial position of the current density, ΔV is the grid volume. All the perturbation contributions from individuals are summed over all the grid volumes, and are accumulated to be the *Dst* index Dst_{MHD}. The temporal resolution of the index is determined by the current density $\boldsymbol{j}$, which depends on the arbitrary interval of the data outputs from the simulation. In this work, we choose one minute resolution that is same as that of SYM-*H* index but much smaller than one hour for the standard *Dst* index. For simplicity, we keep the use of the term *Dst* index to represent the simulated one minute resolution *Dst* index in the following content.

2.2 Empirical *Dst* Index from Ring Current

The absence of ring current model in the global MHD model will cause inconsistent result for the estimation of *Dst* index. For instance, the sudden drop of *Dst* index during magnetic storm can not be reproduced in the simulation which mostly depends on the enhancement of ring current in the inner magnetosphere (Rastätter et al., 2013). Rae et al. (2010) demonstrated that the physics of the inner magnetosphere plays a critical role in shaping the boundary between open and closed field lines during periods of southward interplanetary magnetic field in global simulations. In order to overcome this discrepancy, a physics-based inner magnetospheric model with embedded ring current needs be integrated into an existing global MHD model of magnetosphere (De Zeeuw, 2004). Here we try a different approach with an empirical model. Burton et al. (1975) presented an algorithm to calculate *Dst* index solely from a knowledge of the solar wind velocity, density and IMF conditions. Their equations for *Dst* index (*Dst* in the equation) are expressed as

$$\frac{\mathrm{d}Dst^*}{\mathrm{d}t} = F(E_y) - aDst^*, \tag{2}$$

$$Dst^* = Dst - b\sqrt{P_{\text{dyn}}} + c, \tag{3}$$

where $a = 3.6 \times 10^{-5}\ \text{s}^{-1}$ is the coefficient related to the decay time of the ring current particles; P_{dyn} stands for the dynamic pressure of solar wind; $b = 0.2\ \text{nT}(\text{eV/cm}^3)^{1/2}$ and $c = 20$ nT are coefficients measuring the *Dst* response to solar wind dynamic pressure P_{dyn} and the quiet-time ring current, respectively. $F(E_y)$ represents the ring current injection rate as a function of a delayed and filtered solar wind electric field E_y, is set to be

$$F(E_y) = \begin{cases} 0 & E_y < 0.5\ \ \text{mV/m} \\ d(E_y - 0.5) & E_y > 0.5\ \ \text{mV/m} \end{cases}, \tag{4}$$

where $d = -1.5 \times 10^{-3}\ (\text{nT} \cdot \text{m})/(\text{mV} \cdot \text{s})$ is a constant used to measure the degree of response of injection rate to E_y, assuming that this response is linear. The physical meaning of $F(E_y)$ is to represent the injection of particles into the ring current, which is a function of the rate at which the ring current is enhanced by the solar wind electric field in the dawn–dusk direction.

In the global MHD model, the y component of solar wind electric field is directly calculated from the undisturbed solar wind velocity $\boldsymbol{v}$ and the magnetic field $\boldsymbol{B}$ at the $x = 0$ plane in the GSM coordinate system:

$$E_y = v_x B_z - v_z B_x. \tag{5}$$

Once E_y and the corresponding injection rate F are obtained, Equations (2) and (3) are then discretized to achieve the empirical *Dst* index (Dst_{E} in the equation) in time as

$$Dst_{\text{E}}(t^{n+1}) = Dst_{\text{E}}(t^n) + \Delta t[F^n(E_y) - \frac{a}{2}(Dst_{\text{E}}(t^n) - b\sqrt{P_{\text{dyn}}} + c)]. \tag{6}$$

Note that the effects of global magnetospheric current densities on the *Dst* index have been simulated in the global MHD model, we may consider the contribution solely from the ring currents, so that the solar wind dynamic pressure component is neglected by means of $b = 0$. Finally, we obtain the following equation

$$Dst_{\text{E}}(t^{n+1}) = Dst_{\text{E}}(t^n) + \Delta t[F^n(E_y) - \frac{a}{2}(Dst_{\text{E}}(t^n) + c)]. \tag{7}$$

In this way, the ring current-dependent *Dst* index has been calculated by the above numerical implementation, and is added to the *Dst* index from the MHD model as the final result.

$$Dst = Dst_{\text{MHD}} + Dst_{\text{E}}. \tag{8}$$

Note that the empirical component Dst_{E} cannot produce positive values, nor does it accurately predict the sudden commencement of the *Dst* index during the onset of geomagnetic storms. However, the MHD component Dst_{MHD} can effectively simulates the *Dst* variations caused by the change of solar wind dynamical pressure. Therefore, this semi-empirical model, combining the two *Dst* contributions from the MHD-based magnetospheric currents and the empirical ring current, is expected to enhance the overall simulation performance during geomagnetic storm time. The detailed performance of the model compared with observations will be presented in the following contents.

3. Events and Analysis Methods

There are totally fifteen magnetic storm events selected for analysis: ten categorized as moderate magnetic storms and the remaining five as intense magnetic storms. Table 1 provides the details on all the moderate and intense magnetic storms, including their initiation dates and the respective minimum values of the SYM-*H* index.

All these events occurred from the year of 2021 to 2023, with a separation line of −100 nT between moderate and intense magnetic storms. For these events, the one-minute resolution time-varying solar wind data from OMNI database (https://omniweb.gsfc.nasa.gov/), including density, velocity, magnetic field, and temperature, are used to drive the global MHD simulation at the front boundary at $x = 30R_E$. The output data of the simulation has same temporal resolution as the solar wind input, the simulated one-minute *Dst* index will be compared with the observed SYM-*H* index, which is also obtained from the same database. During the simulation of a geomagnetic storm event, we pre-warm the model one hour ahead of the event's onset. For example, for Event 5, which simulates the entire geomagnetic storm on April 10, 2022, the input solar wind conditions start from 23:00 on April 9, 2022, and end at 00:00 on April 11, 2022. Specifically, the input solar wind conditions are initiated one hour before the event and conclude precisely at the event's end time.

In order to evaluate the performance of the global MHD model, we typically use the four parameters, namely, Prediction Efficiency (PE), Correlation Coefficient (CC), Root Mean Square Error (RMSE) and Central Root Mean Square Error (CRMSE), to assess the simulated *Dst* indices. The PE for discrete time series is defined as a measure that compares the residual variance of the model predictions against the variance of the observed data. It essentially evaluates how well the model can predict the observed values by quantifying the reduction in error variance achieved by using the model compared to simply using the mean of the observed values. It is defined for discrete time series as follows

$$\mathrm{PE} = 1 - \frac{<(x_{\mathrm{mod}} - x_{\mathrm{obs}})^2>}{\sigma_{\mathrm{obs}}^2}, \tag{9}$$

where <···> represents the arithmetic mean, x_{obs} is the observed value, and x_{mod} the modeled signal, σ_{obs} the standard deviation (STD) of the observed values. A higher PE indicates better model performance, a PE value of 1 signifies a perfectly accurate model, whereas a PE of 0 indicates a model's performance equivalent to simply using the arithmetic mean of the observed signals. So that PE less than or equal to zero does not provide useful predictions of the time variation of the observations.

The CC serves as an indicator measuring the extent of linear correlation between two variables. Here we have the expression as follows:

$$\mathrm{CC} = \frac{<(x_{\mathrm{obs}} - \bar{x}_{\mathrm{obs}})(x_{\mathrm{mod}} - \bar{x}_{\mathrm{mod}})>}{\sigma_{\mathrm{obs}}\sigma_{\mathrm{mod}}}, \tag{10}$$

where $\bar{x}$ is the average value, σ_{mod} represents the STD of the simulated values. CC spans a range from −1 to 1. A CC of 1 signifies a perfect positive linear relationship, while a CC of −1 indicates a perfect negative one. A value near zero suggests no significant linear relationship exists.

The RMSE represents the sample standard deviation of the residuals (prediction errors). Residuals are a measure of how far away each observed data point is from the prediction made by the model. Mathematically, RMSE is calculated as follows:

$$\mathrm{RMSE} = \sqrt{\frac{1}{N}\sum (x_{\mathrm{mod}} - x_{\mathrm{obs}})^2}. \tag{11}$$

The size of RMSE provides insight into the accuracy of a model's predictions. Comparing RMSE values across different models predicting the same outcome can help determine which model performs better. A lower RMSE generally indicates superior performance.

The CRMSE is a metric used to assess the accuracy of predictions in a model, particularly when dealing with spatial or geostatistical data. Unlike RMSE, which calculates the square root of the average of squared differences between predicted and observed values over all data points, the CRMSE focuses on evaluating the error at a central or reference location. The formula for calculating CRMSE is as follows:

$$\mathrm{CRMSE} = \sqrt{\frac{1}{N}\sum [(x_{\mathrm{mod}} - \bar{x}_{\mathrm{mod}}) - (x_{\mathrm{obs}} - \bar{x}_{\mathrm{obs}})]^2}. \tag{12}$$

The CRMSE is calculated after centering both the predictions and observations around their respective means, which essentially removes any constant difference between them. A smaller CRMSE indicates that the model's predictions are closer to the actual values once the systematic bias has been accounted for. This suggests better performance of the model in terms of precision

Table 1. Start date of all moderate magnetic storm (1−10) and intense storm (11−15) events and the corresponding minimum of SYM-*H* index.

Event number	Start date	Minimum (nT)
1	2021-02-28	−80
2	2021-03-19	−60
3	2021-09-17	−73
4	2022-03-05	−60
5	2022-04-10	−67
6	2022-07-01	−67
7	2022-10-14	−78
8	2022-12-07	−68
9	2023-06-15	−84
10	2023-09-12	−84
11	2022-03-13	−114
12	2023-03-23	−170
13	2023-10-21	−108
14	2023-11-25	−109
15	2023-12-01	−136

around the mean of the data. Conversely, a larger CRMSE suggests that there is more variability between the predictions and the true values, indicating poorer performance. Through the model evaluation parameters introduced above, we will conduct predictive performance evaluations on all the listed events.

4. Simulation Results

In this section, we will present and analyze the simulation results compared to observations for several specific geomagnetic storm events listed in Table 1. Figure 1 shows the comparison results among the simulations and observation for the three magnetic storm events of Event 5, 11, and 15 listed in the table. The green, blue, red lines indicate the results from the simulations of the MHD, empirical, and semi-empirical models, respectively. The black line depicts the observed SYM-*H* data sourced from the OMNI database.

Figure 1a shows the results for the event occurred on April 10, 2022, with the minimum SYM-*H* value of −67 nT at round 6:45. Compared with the observation, it is evident that the MHD model effectively simulates the substantial pulse in the *Dst* index during the sudden commencement of the magnetic storm at around 2:55, and followed by the similar small-scale fluctuations during the subsequent decline phase, although the overall decreases of the *Dst* index are not reproduced due to the absence of ring current. This result confirms that the standalone MHD model is not sufficient for the calculation of *Dst* index. Compared with the MHD simulation, the overall trend of the empirical results coincide with the observation much better, the valley of *Dst* variation is well reproduced; however, the obtained values are less than the observed before round 5:10, and after that, the former becomes larger than the latter with a difference of around 5–20 nT. As a comparison, the semi-empirical results seem more closely align with observed data, demonstrating better performance throughout both the sharp drop and recovery stages of the magnetic storm. Details of the performance metrics for this event can be

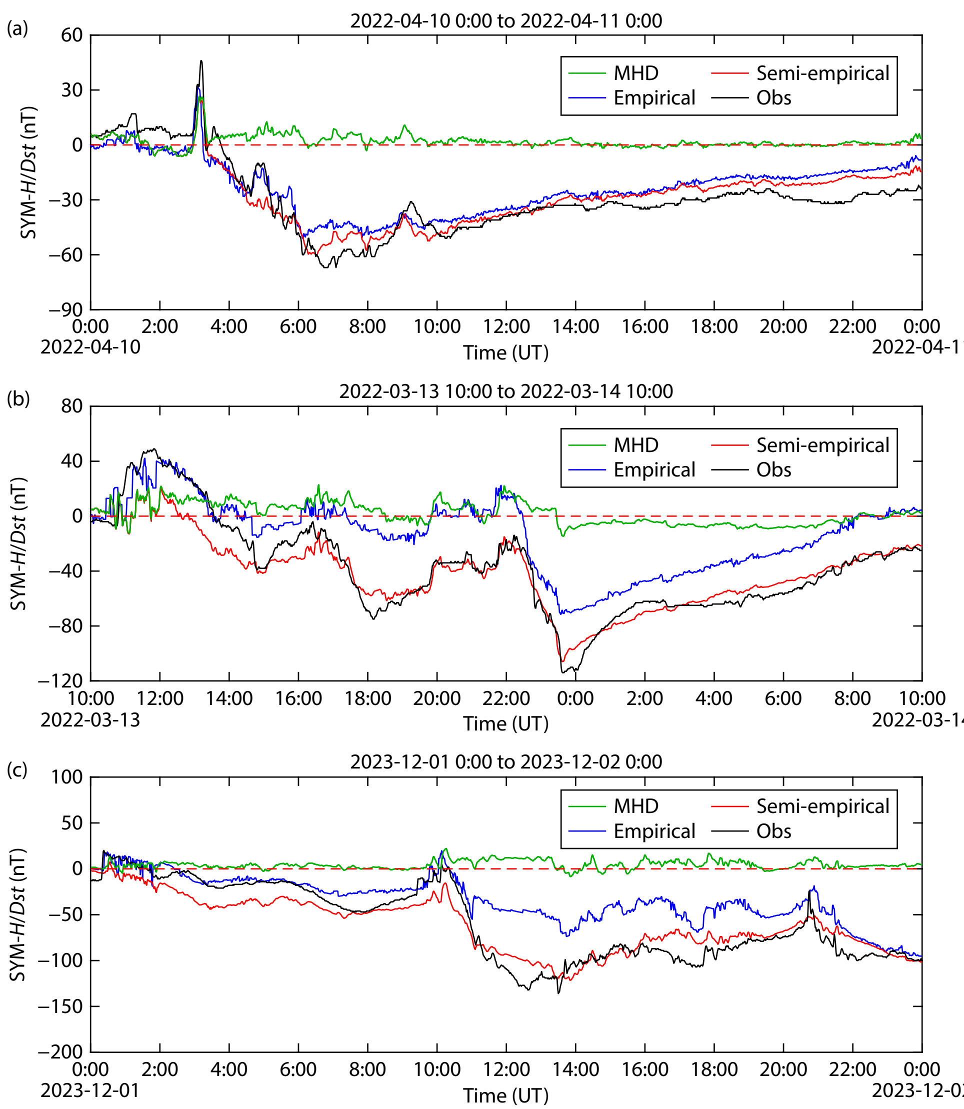

Figure 1. Panels a, b and c show the comparisons among the simulation and observation data, respectively correspond to Event 5, 11, and 15 in Table 1. The MHD-based, empirical and semi-empirical one-minute *Dst* indices are depicted by the green, blue, and red lines, respectively. The black line shows the observed SYM-*H* index obtained from the OMNI database. The red dashed line indicates the zero value for SYM-*H*/*Dst* indices.

found in Table 2, affirming the semi-empirical results globally improve the simulation accuracy for the index concerning this moderate magnetic storm event.

The comparison results for the intense geomagnetic storm that occurred on March 13, 2022, corresponding to Event 11 in Table 1, are presented in Figure 1b. This intense storm is more complicated than the one in panel (c), showing that it has three steps with decreasing minimum *Dst* values of −39 nT, −75 nT and −114 nT at around 14:48, 18:09 and 23:37, respectively. Compared with the observation, the MHD simulation captures the similar tendency but much less amplitutde in the *Dst* index during the whole period. Notice that the negative *Dst* indices appear during the third main phase and the corresponding recovery phase, which is not seen in panel (a). This phenomenon is caused by the ring current from the MHD simulation, though the current density is much less than expected due to the lack of gradient/curvature drift mechansim in the MHD model. Around 11:00, observational data revealed the sudden commencement of the magnetic storm, a process that was, to some degree, mirrored by our MHD simulation. Another ascent was evident in the observed data at approximately 16:00, which our simulations also managed to replicate. A significant resurgence in the observed values was noted at around 22:00, and this was accurately captured by our MHD simulation. The empirical model adeptly portrays the overarching trends in the *Dst* index fluctuations and succeeds in simulating the observed index's multiple downturns. As a comparison, the semi-empirical data are less accurately predicted during the sudden commencement of the geomagnetic storm around 12:00; however, regarding the entire subsequent progression, the performance of the empirical model is less satisfactory, the semi-empirical model is more closely aligned with the observation. For example, at the three critical time points at approximately 16:00, 22:00, and 00:00, the semi-empirical model exhibits better performance than the empirical one. In this event, the semi-empirical model demonstrates a better forecasting capability, which will be presented in Table 2 as well.

Figure 1c shows the intense geomagnetic storm event on December 1, 2023. In this case, the geomagnetic storm features two rapid onset stages, occurring around 0:20 and 10:00, respectively. Similarly, the MHD simulation captures the sudden commencement at the onset stage, which is mainly caused by the solar wind dynamic pressure changes; the index does not drop as the observation. The empirical model effectively demonstrates the overall trend of *Dst* index and successfully simulates the two declines observed on the panel. The empirical results show a close correlation with the observation, however, the obtained indices are much larger during the main and recovery phases of the storm. The semi-empirical results show a closer match with the observed data, with a much lower *Dst* value during both the main phase and recover phase, indicating that the model performs better as a comparison.

For all the listed 15 events, Table 2 presents the performance evaluation parameters, including PE, CC, RMSE, and CRMSE. Among all the events, the lowest PE is 0.55 for Event 3, with most events achieving a PE above 0.7. The lowest CC of 0.89 occurs for Event 8, and the rest are above 0.9. Moreover, the RMSE and CRMSE metrics also reflect strong predictive performance, with values typically not surpassing 15, which is a favorable value for the index prediction. In contrast, the empirical model quantitatively shows the poorer performances, being with negative PE values in Events 3, 8, and 14, and most PEs below 0.7; the CCs are less than 0.8 in Events 3, 10, and 13. The RMSE and CRMSE metrics are generally much larger than those for the semi-empirical model. The results indicate that the semi-empirical model performs better than the empirical one in predicting the *Dst* index for both

Table 2. Summary of simulation performance evaluation parameters for the comparison of the empirical and semi-empirical models with SYM-*H* observations in all moderate and intense magnetic storm events.

Event number	Start date	Minimum (nT)	Semi-empirical				Empirical			
			PE	CC	RMSE	CRMSE	PE	CC	RMSE	CRMSE
1	2021-02-28	−80	0.86	0.96	9.9	8.6	0.83	0.95	11	9.8
2	2021-03-19	−60	0.76	0.94	15	12	0.61	0.96	20	14
3	2021-09-17	−73	0.55	0.90	13	9.9	−0.95	0.71	27	14
4	2022-03-05	−60	0.63	0.94	12	9.2	0.86	0.94	7.1	6.3
5	2022-04-10	−67	0.84	0.93	7.8	7.6	0.72	0.91	10	8.9
6	2022-07-01	−67	0.72	0.97	15	7.5	0.76	0.97	14	11
7	2022-10-14	−78	0.83	0.92	8.0	8.0	0.76	0.87	9.5	9.5
8	2022-12-07	−68	0.62	0.89	10	10	−0.24	0.93	19	6.6
9	2023-06-15	−84	0.63	0.90	18	13	0.56	0.92	19	13
10	2023-09-12	−84	0.69	0.96	15	7.9	0.50	0.77	19	17
11	2022-03-13	−114	0.85	0.95	13	13	0.26	0.89	29	16
12	2023-03-23	−170	0.75	0.98	28	18	0.74	0.90	29	28
13	2023-10-21	−108	0.77	0.92	14	12	0.31	0.79	24	18
14	2023-11-25	−109	0.66	0.90	13	12	−0.54	0.92	29	11
15	2023-12-01	−136	0.85	0.95	16	16	0.33	0.87	33	22

moderate and intense geomagnetic storms. There is no significant disparity in the predictive performance between moderate and intense geomagnetic storms according to these evaluation parameters. This consistency in forecasting performance extends even to intense geomagnetic storm events with *Dst* values as low as −170 nT, where the forecast remains robust.

Figure 2 illustrates scatter plots of the SYM-*H* indices against the simulated *Dst* values after following the integration of multiple events. In panel (a), data points from ten moderate geomagnetic storm events are plotted on the same plane. The red dashed line indicate the positions where the observation and simulation coincide with each other. It is evident that the simulation results from the semi-empirical model exhibit a robust linear correlation with the observed data, with the points being evenly distributed around the red dashed line, showing good agreements between the two kinds of values. For panel (b), the simulation data are produced from the standalone MHD model for all moderate geomagnetic storms. Without the embedded empirical ring current model, the simulation results mainly vary between −10 nT and 20 nT. This off-red dashed line distribution reconfirm that the MHD simulations are unable to accurately replicate the ring current, resulting in an inability to simulate a significantly decreased SYM-*H* index. In panel (c), the integrated data points from five intense geomagnetic storm events are presented. The simulation results from the semi-empirical model maintain a strong linear relationship with the observed data during these intenser events. Notably, once the observed SYM-*H* index reaches approximately −120 nT, the simulated values from the semi-empirical model tend to underestimate the observed data, showing some inefficiency in producing the *Dst* indices for intense magnetic storms. Lastly, panel (d) displays the MHD model's simulation results for intense geomagnetic storms. Similar to the moderate storms, the simulated values are mostly confined within the range, showing the limitation of MHD model in capturing the dynamics of the ring current during intense geomagnetic disturbances.

In order to test the accuracy performance of the semi-empirical model under extremely intense geomagnetic conditions, we present the model result for the super geomagnetic storm event that occurred on May 10, 2024. The results are shown in Figure 3, where the lowest observed SYM-*H* index reached −518 nT at 2:14 on the next day. Both the empirical and semi-empirical models successfully reproduced the occurrence of the super geomagnetic storm, being with only minor differences in specific details. For the period of rapid decline in data from 18:00 on May 10th to 2:00 on May 11th, the predictions made by the semi-empirical model were more closely aligned with the observed data, indicating that the semi-empirical model performs more accurately during the main phase of magnetic storms. In the subsequent recovery phase, however, there are significant discrepancies between the

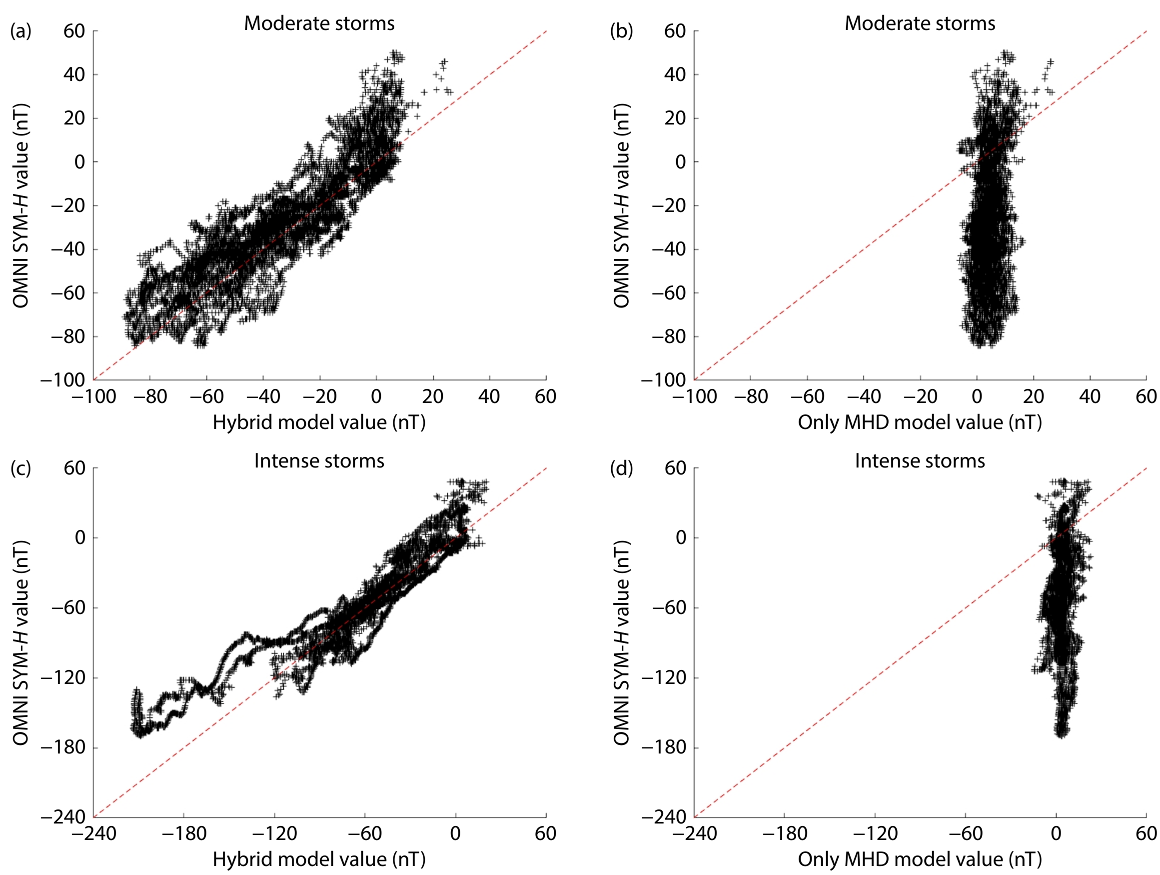

Figure 2. Scatter plots of the observed SYM-*H* indices from the OMNI database versus the simulated values from (a) the semi-empirical model for 10 moderate magnetic storm events, (b) the standalone MHD model for 10 moderate magnetic storm events, (c) the semi-empirical model for 5 intense magnetic storm events, and (d) the standalone MHD model for 5 intense magnetic storm events.

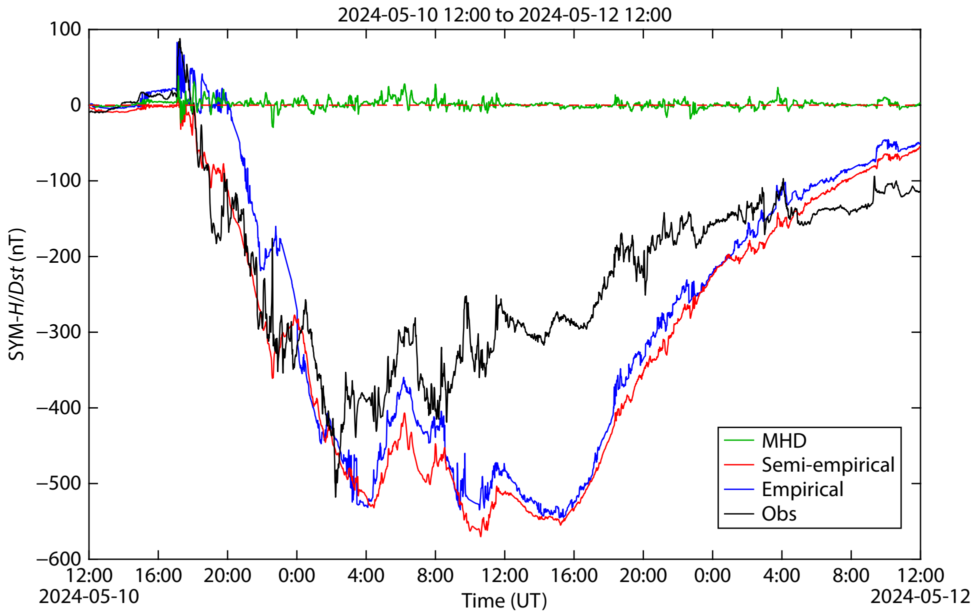

Figure 3. Comparison between the observation and the simulations for the super geomagnetic storm on May 10, 2024.

modelings and observation, both models do not recover in phase with the observation after around 7:00 until at round 5:00 on the next day. This late-recovery result may be caused the choice of coefficient *a* in Equation (2), which measures the decay time of the ring current particles. This highlights an area for potential improvement in our models, aiming to enhance its ability to predict the recovery phase of super geomagnetic storms. Nevertheless, the fact that the semi-empirical model could successfully and closely predict the lowest value of the SYM-*H* index suggests it has considerable potential for simulating super geomagnetic storms.

5. Summary

In this study, we have developed a semi-empirical model for the *Dst* index prediction based on the global MHD simulation of Earth's magnetosphere. In this model, the contribution of the ring current to *Dst* index is estimated using an existing empirical formula, while the effects of other current systems are still derived from the MHD simulations. The performance of the semi-empirical model was evaluated against the observation and that of Burton's empirical model, through a comprehensive analysis involving multiple performance assessment metrics. It has been demonstrated that, in the context of moderate and intense geomagnetic storm events, the semi-empirical model significantly outperforms the original empirical methods. Furthermore, it compensates, to some extent, for the shortcomings of the global MHD model of Earth's magnetosphere that does not include the ring current. Moreover, compared with the physics-based ring current model, this model is much less time-comsuming and easier to be implemented in a global MHD model. Thus, it is suitable to utilize this semi-empirical model in a global MHD model of Earth's magnetosphere for the *Dst* index forecasting in the practical use of space weather services.

Acknowledgments

This work was supported by NNSFC grants 42150101, 42188105, 42304189, National Key R&D program of China No.2021YFA-0718600, and the Pandeng Program of National Space Science Center, Chinese Academy of Sciences. We acknowledge the use of NASA/GSFC's Space Physics Data Facility's OMNIWeb service and OMNI data. *Dst* index, SYM-*H* index and solar wind data are publicly available from NASA's National Space Science Data Center (https://nssdc.gsfc.nasa.gov/).

References

Burton, R. K., McPherron, R. L., and Russell, C. T. (1975). An empirical relationship between interplanetary conditions and *Dst*. *J. Geophys. Res.*, *80*(31), 4204–4214. https://doi.org/10.1029/JA080i031p04204

Buzulukova, N., Fok, M. C., Pulkkinen, A., Kuznetsova, M., Moore, T. E., Glocer, A., Brandt, P. C., Tóth, G., and Rastätter, L. (2010). Dynamics of ring current and electric fields in the inner magnetosphere during disturbed periods: CRCM–BATS-R-US coupled model. *J. Geophys. Res.: Space Phys.*, *115*(A5), A05210. https://doi.org/10.1029/2009JA014621

Camporeale, E. (2019). The challenge of machine learning in space weather: Nowcasting and forecasting. *Space Weather*, *17*(8), 1166–1207. https://doi.org/10.1029/2018SW002061

Caswell, J. M. (2014). A nonlinear autoregressive approach to statistical prediction of disturbance storm time geomagnetic fluctuations using solar data. *J. Signal Inf. Process.*, *5*(2), 42–53. https://doi.org/10.4236/jsip.2014.52007

Cramer, W. D., Turner, N. E., Fok, M. C., and Buzulukova, N. Y. (2013). Effects of different geomagnetic storm drivers on the ring current: CRCM results. *J. Geophys. Res.: Space Phys.*, *118*(3), 1062–1073. https://doi.org/10.1002/jgra.50138

Dessler, A. J., and Parker, E. N. (1959). Hydromagnetic theory of geomagnetic storms. *J. Geophys. Res.*, *64*(12), 2239–2252. https://doi.org/10.1029/JZ064i012p02239

De Zeeuw, D. L., Sazykin, S., Wolf, R. A., Gombosi, T. I., Ridley, A. J., and Tóth, G. (2004). Coupling of a global MHD code and an inner magnetospheric model: Initial results. *J. Geophys. Res.: Space Phys.*, *109*(A12), A12219. https://doi.org/10.1029/2003JA010366

Gleisner, H., Lundstedt, H., and Wintoft, P. (1996). Predicting geomagnetic storms from solar-wind data using time-delay neural networks. *Ann. Geophys.*, *14*(7), 679–686. https://doi.org/10.1007/s00585-996-0679-1

Guo, X. C. (2015). An extended HLLC Riemann solver for the magneto-hydrodynamics including strong internal magnetic field. *J. Comput. Phys.*, *290*, 352–363. https://doi.org/10.1016/j.jcp.2015.02.048

Guo, X. C., Florinski, V., and Wang, C. (2016). The HLLD Riemann solver based on magnetic field decomposition method for the numerical simulation of magneto-hydrodynamics. *J. Comput. Phys.*, *327*, 543–552. https://doi.org/10.1016/j.jcp.2016.09.057

Hill, T. (1984). Magnetic coupling between solar wind and magnetosphere: Regulated by ionospheric conductance. *Eos Trans. AGU*, *65*(45), 1047.

Hilmer, R. V., and Voigt, G. H. (1995). A magnetospheric magnetic field model with flexible current systems driven by independent physical parameters. *J. Geophys. Res.: Space Phys.*, *100*(A4), 5613–5626. https://doi.org/10.1029/94JA03139

Horton, W., and Doxas, I. (1998). A low-dimensional dynamical model for the solar wind driven geotail-ionosphere system. *J. Geophys. Res.: Space Phys.*, *103*(A3), 4561–4572. https://doi.org/10.1029/97JA02417

Hu, Y. Q., Guo, X. C., and Wang, C. (2007). On the ionospheric and reconnection potentials of the Earth: Results from global MHD simulations. *J. Geophys. Res.: Space Phys.*, *112*(A7), A07215. https://doi.org/10.1029/2006JA012145

Iyemori, T. (1990). Storm-time magnetospheric currents inferred from mid-latitude geomagnetic field variations. *J. Geomag. Geoelectr.*, *42*(11), 1249–1265. https://doi.org/10.5636/jgg.42.1249

Jankovičová, D., Dolinský, P., Valach, F., and Vörös, Z. (2002). Neural network-based nonlinear prediction of magnetic storms. *J. Atmos. Sol. Terr. Phys.*, *64*(5-6), 651–656. https://doi.org/10.1016/S1364-6826(02)00025-1

Jordanova, V. K., Zaharia, S., and Welling, D. T. (2010). Comparative study of ring current development using empirical, dipolar, and self-consistent magnetic field simulations. *J. Geophys. Res.: Space Phys.*, *115*(A12), A00J11. https://doi.org/10.1029/2010JA015671

Kugblenu, S., Taguchi, S., and Okuzawa, T. (1999). Prediction of the geomagnetic storm associated D_{st} index using an artificial neural network algorithm. *Earth Planets Space*, *51*(4), 307–313. https://doi.org/10.1186/BF03352234

Lazzús, J. A., Vega, P., Rojas, P., and Salfate, I. (2017). Forecasting the *Dst* index using a swarm-optimized neural network. *Space Weather*, *15*(8), 1068–1089. https://doi.org/10.1002/2017SW001608

Lethy, A., El-Eraki, M. A., Samy, A., and Deebes, H. A. (2018). Prediction of the *Dst* index and analysis of its dependence on solar wind parameters using neural network. *Space Weather*, *16*(9), 1277–1290. https://doi.org/10.1029/2018SW001863

Liemohn, M., Ganushkina, N. Y., De Zeeuw, D. L., Rastaetter, L., Kuznetsova, M., Welling, D. T., Toth, G., Ilie, R., Gombosi, T. I., and van der Holst, B. (2018). Real-time SWMF at CCMC: Assessing the Dst output from continuous operational simulations. *Space Weather*, *16*(10), 1583–1603. https://doi.org/10.1029/2018SW001953

Lu, J. Y., Peng, Y. X., Wang, M., Gu, S. J., and Zhao, M. X. (2016). Support vector machine combined with distance correlation learning for *Dst* forecasting during intense geomagnetic storms. *Planet. Space Sci.*, *120*, 48–55. https://doi.org/10.1016/j.pss.2015.11.004

Lundstedt, H., and Wintoft, P. (1994). Prediction of geomagnetic storms from solar wind data with the use of a neural network. *Ann. Geophys.*, *12*(1), 19–24. https://doi.org/10.1007/s00585-994-0019-2

Lundstedt, H., Gleisner, H., and Wintoft, P. (2002). Operational forecasts of the geomagnetic *Dst* index. *Geophys. Res. Lett.*, *29*(24), 2181. https://doi.org/10.1029/2002GL016151

Lyon, J. G., Fedder, J. A., and Mobarry, C. M. (2004). The Lyon–Fedder–Mobarry (LFM) global MHD magnetospheric simulation code. *J. Atmos. Sol. Terr. Phys.*, *66*(15-16), 1333–1350. https://doi.org/10.1016/j.jastp.2004.03.020

Maharana, A., Scolini, C., Raeder, J., and Poedts, S. (2021). Predicting geo-effectiveness of CMEs with EUHFORIA coupled to OpenGGCM. https://doi.org/10.5194/egusphere-egu21-9854

Morley, S. K., Jordanova, V. K., Zheng, Y. H., and Petrenko, M. (2023). RAM-SCB runs on request at CCMC. *Space Weather*, *21*(12), e2023SW003771. https://doi.org/10.1029/2023SW003771

O'Brien, T. P., and McPherron, R. L. (2000). Forecasting the ring current index *Dst* in real time. *J. Atmos. Sol. Terr. Phys.*, *62*(14), 1295–1299. https://doi.org/10.1016/S1364-6826(00)00072-9

Park, W., Lee, J., Kim, K. C., Lee, J., Park, K., Miyashita, Y., Sohn, J., Park, J., Kwak, Y. S., ... Yi, Y. (2021). Operational Dst index prediction model based on combination of artificial neural network and empirical model. *J. Space Weather Space Clim.*, *11*, 38. https://doi.org/10.1051/swsc/2021021

Rae, I. J., Kabin, K., Lu, J. Y., Rankin, R., Milan, S. E., Fenrich, F. R., Watt, C. E. J., Zhang, J. C., Ridley, A. J., ... DeZeeuw, D. L. (2010). Comparison of the open-closed separatrix in a global magnetospheric simulation with observations: The role of the ring current. *J. Geophys. Res.: Space Phys.*, *115*(A8), A08216. https://doi.org/10.1029/2009JA015068

Raeder, J., Wang, Y. L., and Fuller-Rowell, T. J. (2001). Geomagnetic storm simulation with a coupled magnetosphere-ionosphere-thermosphere model. *Space Weather*, *125*, 377–384. https://doi.org/10.1029/GM125p0377

Rastätter, L., Kuznetsova, M. M., Glocer, A., Welling, D., Meng, X., Raeder, J., Wiltberger, M., Jordanova, V. K., Yu, Y., ... Gannon, J. (2013). Geospace environment modeling 2008–2009 challenge: D_{st} index. *Space Weather*, *11*(4), 187–205. https://doi.org/10.1002/swe.20036

Sckopke, N. (1966). A general relation between the energy of trapped particles and the disturbance field near the earth. *J. Geophys. Res.*, *71*(13), 3125–3130. https://doi.org/10.1029/JZ071i013p03125

Siscoe, G. L. (1982). Polar cap size and potential: A predicted relationship. *Geophys. Res. Lett.*, *9*(6), 672–675. https://doi.org/10.1029/GL009i006p00672

Spencer, E., Vadepu, S. K., Srinivas, P., Patra, S., and Horton, W. (2018). The dynamics of geomagnetic substorms with the WINDMI model. *Earth Planets Space*, *70*, 118. https://doi.org/10.1186/s40623-018-0882-9

Sugiura, M. (1960). The average morphology of geomagnetic storms with sudden commencement. Abh. Akd. Wiss. Gottingen (Germany) Math. Phys. KL Son-derheft, 4.

Sugiura, M., Kertz, W., Price, A., and Stone, D. (1964). Hourly values of equatorial *Dst* for the IGY. Pergamon Press.

Toffoletto, F. R., Sazykin, S., Wolf, R. A., Spiro, R. W., Birn, J., De Zeeuw, D. L., Gombosi, T., and Hesse, M. (2001). Modeling the inner magnetosphere with a coupled rice convection model. In *AGU Spring Meeting Abstracts*. AGU. Vol. 2001, pp. SM31B–08.

Tóth, G., Sokolov, I. V., Gombosi, T. I., Chesney, D. R., Clauer, C. R., De Zeeuw, D. L., Hansen, K. C., Kane, K. J., Manchester, W. B., ... Kóta, J. (2005). Space weather modeling framework: A new tool for the space science community. *J. Geophys. Res.: Space Phys.*, *110*(A12), A12226. https://doi.org/10.1029/2005JA011126

Turner, N. E., Baker, D. N., Pulkkinen, T. I., and McPherron, R. L. (2000). Evaluation of the tail current contribution to *Dst*. *J. Geophys. Res.: Space Phys.*, *105*(A3), 5431–5439. https://doi.org/10.1029/1999JA000248

Vasyliunas, V. M. (1970). Mathematical models of magnetospheric convection and its coupling to the ionosphere. In *Particles and Fields in the Magnetosphere* (pp. 60-71). Santa Barbara, CA, USA: Springer. https://doi.org/10.1007/978-94-010-3284-1_6

Wang, C. B., Chao, J. K., and Lin, C. H. (2003). Influence of the solar wind dynamic pressure on the decay and injection of the ring current. *J. Geophys. Res.: Space Phys.*, *108*(A9), 1341. https://doi.org/10.1029/2003JA009851

Wanliss, J. A., and Showalter, K. M. (2006). High-resolution global storm index: *Dst* versus SYM-H. *J. Geophys. Res.: Space Phys.*, *111*(A2), A02202. https://doi.org/10.1029/2005JA011034

Weimer, D. R. (2005). Improved ionospheric electrodynamic models and application to calculating joule heating rates. *J. Geophys. Res.: Space Phys.*, *110*(A5), A05306. https://doi.org/10.1029/2004JA010884

Wolf, R. A., Spiro, R. W., and Rich, F. J. (1991). Extension of convection modeling into the high-latitude ionosphere: Some theoretical difficulties. *J. Atmos. Terr. Phys.*, *53*(9), 817–829. https://doi.org/10.1016/0021-9169(91)90096-P

Wu, J. G., and Lundstedt, H. (1997). Geomagnetic storm predictions from solar wind data with the use of dynamic neural networks. *J. Geophys. Res.: Space Phys.*, *102*(A7), 14255–14268. https://doi.org/10.1029/97JA00975

Xu, S. B., Huang, S. Y., Yuan, Z. G., Deng, X. H., and Jiang, K. (2020). Prediction of the Dst index with bagging ensemble-learning algorithm. *Astrophys. J. Suppl. Ser.*, *248*, 14. https://doi.org/10.3847/1538-4365/ab880e

Xu, W. W., Zhu, Y. M., Zhu, L., Lu, J. Y., Wei, G. C., Wang, M., and Peng, Y. X. (2023). A class of Bayesian machine learning model for forecasting Dst during intense geomagnetic storms. *Adv. Space Res.*, *72*(9), 3882–3889. https://doi.org/10.1016/j.asr.2023.07.009